

manuscript submitted to *JGR: Solid Earth*

1 **Evidence for deeply-subducted lower-plate seamounts
2 at the Hikurangi subduction margin: implications for
3 seismic and aseismic behavior**

4 **Bryant Chow^{1,2}, Yoshihiro Kaneko³, John Townend¹**

5 ¹School of Geography, Environment and Earth Sciences, Victoria University of Wellington

6 ²GNS Science

7 ³Department of Geophysics, Kyoto University

8 **Key Points:**

- 9 • We image velocity anomalies below the North Island, New Zealand, interpreted
10 as deeply-subducted seamounts and fluid in the downgoing plate
- 11 • Independent geological and geophysical observations corroborate our seamount in-
12 terpretation
- 13 • Inferred seamounts and intraslab fluid may partly explain enigmatic, along-strike
14 plate-coupling transition at the Hikurangi margin

Corresponding author: Bryant Chow, bryant.chow@vuw.ac.nz

15 **Abstract**

16 Seamounts are found at many global subduction zones and act as seafloor heterogeneities
 17 that affect slip behavior on megathrusts. At the Hikurangi subduction zone offshore the
 18 North Island, New Zealand, seamounts have been identified on the incoming Pacific plate
 19 and below the accretionary prism, but there is little concrete evidence for seamounts sub-
 20 ducted past the present day coastline. Using a high-resolution, adjoint tomography-derived
 21 velocity model of the North Island, New Zealand we identify two high-velocity anomalies
 22 below the East Coast and an intraslab low-velocity zone up-dip of one of these anom-
 23 alies. We interpret the high-velocity anomalies as two previously-unidentified, deeply-subducted
 24 seamounts, and the low-velocity zone as fluid in the subducting slab. The seamounts are
 25 inferred to be 10–30km wide and on the plate interface at 12–15km depth. Resolution
 26 analysis using point spread functions confirm that these are well-resolved features. The
 27 locations of the two seamounts correlate with bathymetric features whose geometries are
 28 consistent with those predicted from analog seamount subduction experiments. The spa-
 29 tial characteristics of seismicity and slow slip events near the inferred seamounts agree
 30 well with previous finite element modeling predictions on the effects of seamount sub-
 31 duction on megathrust stress and slip. Anomalous geophysical signatures, magnetic anom-
 32 alies, and swarm seismicity have also been observed previously at one or both seamount
 33 locations. We propose that permanent fracturing of the northern Hikurangi upper plate
 34 by repeated seamount subduction may be responsible for the dichotomous geodetic be-
 35 havior observed, and partly responsible for along-strike variations in plate coupling on
 36 the Hikurangi subduction interface.

37 **Plain Language Summary**

38 Seamounts are large volcanic edifices on the seafloor that eventually make their way
 39 into subduction zones. Seamounts have been identified at various stages of subduction
 40 and are thought to either promote or suppress the occurrence of large earthquakes at sub-
 41 duction zones. It is difficult to track seamounts far into a subduction zone due to the
 42 decreasing sensitivity of most geophysical measurements with increasing depth. In this
 43 study, we identify several distinctive seismic velocity anomalies in a high-resolution 3D
 44 model of the North Island, New Zealand. The model is derived using a form of seismic
 45 imaging that improves fits between observed and simulated seismic waveforms. We
 46 interpret the anomalies to indicate the presence of two deeply-subducted seamounts and
 47 fluid in the downgoing plate. The two seamounts are inferred to be at interface depths,
 48 with horizontal dimensions of about 10-30km. These features are well resolved and our
 49 interpretations are supported by independent evidence including seafloor bathymetry data
 50 and the presence of nearby geophysical anomalies. We associate these seamounts with
 51 variations in slip behavior observed along the Hikurangi subduction margin and propose
 52 that they have caused permanent damage to the upper plate, thereby reducing its abil-
 53 ity to store energy and produce large earthquakes.

54 **1 Introduction**

55 Seamounts are prominent seafloor features found globally at convergent margins,
 56 where their eventual subduction has been observed to have significant effect on upper
 57 plate morphology, and is predicted to influence megathrust slip behaviour. While shal-
 58 low subduction of partially buried seamounts has been inferred to play a role in tectonic
 59 erosion and deformation of the upper plate (e.g., Dominguez et al., 1998; Von Huene &
 60 Scholl, 1991), less is known about what happens as a seamount subducts further because
 61 of the limited resolution of geophysical methods commonly used to identify subducting
 62 seamounts. Previous studies have imaged buried seamounts at shallow stages of subduc-
 63 tion (e.g., Bangs et al., 2006; Pedley et al., 2010; Marcaillou et al., 2016; Frederik et al.,

64 2020) and, in more limited cases, deeper into subduction zones (e.g., Kodaira et al., 2000;
 65 Singh et al., 2011).

66 Arguments linking subducted seamounts to large-earthquake seismogenesis are at
 67 first glance discordant, suggesting either that seamounts facilitate seismic rupture by acting
 68 as locally locked asperities on which large earthquakes can nucleate (Scholz & Small,
 69 1997), or that they impede seismic rupture by fracturing the upper plate and rendering
 70 it incapable of storing sufficient elastic strain to produce large earthquakes (Wang & Bilek,
 71 2011). A number of ideas have been proposed regarding the effects of seamounts on me-
 72 chanical and hydrological processes in the upper plate, which may explain how subducted
 73 seamounts promote both seismic and aseismic behavior (Sun et al., 2020), allow for the
 74 subduction and compaction of additional sediments to depth (Ellis et al., 2015), act as
 75 rupture barriers for large earthquakes (Yang et al., 2013), and transport inordinate amounts
 76 of fluid into subduction zones (Bell et al., 2010; Chesley et al., 2021). However, the small
 77 number of documented examples of deep seamount subduction makes it difficult to re-
 78 solve the complex relationship between seamounts and slip behavior at subduction zones.

79 In Chow et al. (companion manuscript) we use adjoint tomography, an imaging tech-
 80 nique that involves fitting short-period (> 4 s) earthquake-generated seismic waveforms
 81 to corresponding synthetic waveforms, to refine a 3D velocity model of the North Island
 82 of New Zealand (Eberhart-Phillips et al., 2020). Throughout the inversion, strong ve-
 83 locity anomalies in the forearc region are imaged at increasing resolution. Two high-velocity
 84 anomalies are resolved as point-like structures, spanning tens of km, with peaked am-
 85 plitudes at plate interface depths. We also observe a broad low-velocity zone up-dip of
 86 one of these anomalies. Here, we (1) assess the robustness of those velocity anomalies
 87 in more detail, (2) interpret them as prominent tectonic features using corroborating geo-
 88 physical and geological evidence, and (3) discuss the implications of such features for seis-
 89 mic and aseismic behavior at the Hikurangi subduction zone.

90 2 Hikurangi subduction zone

91 The Hikurangi subduction zone is a convergent plate boundary where the Pacific
 92 plate is subducting obliquely westward beneath the Australian plate (Figure 1). The Hiku-
 93 rangi margin exhibits varying differences in along-strike properties (Wallace et al., 2009),
 94 and is commonly separated into northern, central, and southern margins (Figure 1). The
 95 northern section of the margin is characterized by thin incoming sediment cover, a rel-
 96 atively high convergence rate (~ 50 km/yr), and tectonic erosion of the frontal wedge
 97 from repeated seamount subduction, resulting in a steep and narrow accretionary wedge
 98 (20–40 km). Conversely, the central and southern segments exhibit thicker incoming sed-
 99 iment cover (> 5 km), slower (20–40 mm/yr) and increasingly oblique convergence, and
 100 a well-developed, broad, shallow-tapered accretionary wedge (30–70 km) (Barnes et al.,
 101 2010; Wallace, 2020). Although relative plate motion at the Hikurangi subduction zone
 102 is oblique (and increases in obliquity southward), much of the rotational component is
 103 accommodated by right-lateral strike-slip faults in the overlying crust of the North Is-
 104 land (Beanland & Haines, 1998; Wallace et al., 2004, 2009). This has the effect that plate
 105 convergence rates at crustal depths are primarily margin-normal at the trench, with de-
 106 creasing convergence rates from north to south (Figure 2).

107 The incoming seafloor at the northern Hikurangi margin (i.e., north of latitude S40°)
 108 is strewn with seamounts at various stages of subduction. Sediment cover here is rel-
 109 atively thin, and consequently numerous knolls and seamounts are identifiable in high-
 110 resolution bathymetry (Figure 1). Seamounts subducted beneath the accretionary pile
 111 have been imaged using marine seismic reflection surveys (e.g., Barker et al., 2009; Barnes
 112 et al., 2010; Bell et al., 2010). These seamounts are associated with localized uplift of
 113 the seafloor and localized positive magnetic anomalies, and are preceded landward by
 114 high-reflectively zones interpreted to represent underthrust sediment packages (Bell et

115 al., 2010; Ellis et al., 2015). The identified seamounts are typically oblate in shape with
 116 estimated footprints on the scale of tens of kilometers, and heights of less than a few kilo-
 117 meters (Barnes et al., 2010; Bell et al., 2010). Although no seamounts subducted fur-
 118 ther below the North Island have been identified through geophysical methods, some have
 119 been inferred by other means. For example, tectonic reconstructions based on the Poverty
 120 and Ruatoria Re-entrants suggest that very large seamounts have been subducted hun-
 121 dreds of kilometers westward beyond the trench and may currently reside somewhere be-
 122 low the northern North Island (Figure 1; K. B. Lewis et al., 1998; Pedley et al., 2010).

123 The Hikurangi margin presents a rare opportunity to study an active subduction
 124 zone with land-based measurements. The subducting Pacific plate is part of a large igne-
 125 ous province, the Hikurangi plateau, and subduction of this relatively buoyant feature
 126 has caused much of the forearc region to become subaerial (Litchfield et al., 2007; Nicol
 127 et al., 2007). Consequently, the plate interface below the East Coast region is shallow
 128 at 12–15 km depth (Figure 2; Williams et al., 2013). Geodetic inversions used to infer
 129 plate coupling along the interface suggest that the southern Hikurangi margin is geode-
 130 matically locked, while the northern portion is creeping aseismically (Figure 2; Wallace, Bea-
 131 van, et al., 2012; Wallace, 2020). The transition between the two styles of slip occurs across
 132 the central margin (Figure 2) with shallow (5–15 km) slow slip events (SSEs) at the north-
 133 ern margin accommodating the majority of expected plate motion where they occur (Figure 2;
 134 Wallace, 2020). The cause of along-strike differences at the Hikurangi margin is an on-
 135 going topic of research, and a variety of factors including fluids, seamounts, overriding
 136 plate structure, incoming sediment flux, and temperature have been suggested as expla-
 137 nations for the heterogeneous slip behavior observed (Wallace, 2020).

138 3 Data and methods

139 In Chow et al. (companion manuscript) we use earthquake-based adjoint tomog-
 140 raphy to image crustal structure with kilometer-scale resolution at the Hikurangi sub-
 141 duction zone. In adjoint tomography, the misfit between earthquake-generated seismic
 142 waveforms and corresponding wave propagation simulations is minimized in an optimiza-
 143 tion problem. Seismic velocities are iteratively perturbed to reduce this data-synthetic
 144 misfit and improve on an initial velocity model, which in our work is a ray-based 3D to-
 145 mography model of New Zealand (Eberhart-Phillips et al., 2020). The inversion dataset
 146 consists of 60 geographically well-distributed earthquakes, whose waveforms were recorded
 147 at as many as 88 broadband seismometer locations (Figure 1). The total dataset con-
 148 sists of approximately 1800 unique source-receiver pairs. Observed and synthetic wave-
 149 forms are compared using a cross-correlation travelttime misfit at waveform periods of
 150 4–30 s. Adjoint methods are used to derive the gradient of the misfit function, and an
 151 inverse L-BFGS Hessian and backtracking line search are applied to obtain a search di-
 152 rection and step length (Modrak & Tromp, 2016; Chow et al., 2020). In total, 28 iter-
 153 ations are performed, resulting in velocity changes of as much as $\pm 30\%$ with respect to
 154 initial values. The final velocity model is assessed using point spread functions (Fichtner
 155 & Trampert, 2011) and comparisons with known tectonic and geologic features of New
 156 Zealand. In this study, we focus explicitly on velocity anomalies identified in the fore-
 157 arc region of the velocity model. Further elaboration on the inversion and interpreta-
 158 tions of the velocity model as a whole can be found in Chow et al. (companion manuscript).

159 4 Results

160 4.1 East Coast velocity anomalies

161 We identify two high-velocity anomalies below the East Coast and a deep offshore
 162 low-velocity zone (Figure 3). The high-velocity anomalies are located at approximately
 163 plate interface depths (~ 12 –15 km), below Māhia Peninsula (Feature M; Figure 3) and
 164 the North Island township of Pōrangahau (Feature P; Figure 3). The low-velocity zone

165 is located seaward of the Pōrangahau anomaly (Feature O; Figure 3). As shown in Figure
 166 5 of Chow et al. (companion manuscript), these anomalies emerge early in the in-
 167 version process, suggesting that they are required to reduce long-period data–synthetic
 168 misfit. Visualized using a 12 km depth slice through the velocity model (Figure 3A), the
 169 high-velocity anomalies appear circular with $V_s > 3.5$ km/s.

170 The two high-velocity anomalies are distinct with respect to the surrounding ve-
 171 locity structure. In cross-section, they are characterized by bumps of high velocities ($V_s > 3.25$ km/s)
 172 centered at interface depths (Figure 3B, C). The anomaly below Māhia Peninsula shows
 173 a broad region of elevated velocities extending to 20 km depth, almost 10 km below the
 174 assumed plate interface (~12 km). Above the interface, increased velocities can be seen
 175 extending to shallow depths (~5 km; Figure 3B). The Pōrangahau anomaly has a smaller
 176 relative lateral extent, and a more pronounced expression of high velocities extending
 177 upwards to the surface (Figure 3C) and below the subduction interface. A distinctive
 178 difference of the Pōrangahau anomaly is a systematic dip in seismic velocities further sea-
 179 ward, corresponding to the offshore low-velocity zone (Feature O). The two high-velocity
 180 anomalies have similar geometries in a trench-parallel cross-section (Figure 3D).

181 The ratio of seismic velocities (V_p/V_s) is often used to infer the presence of flu-
 182 ids at depth. Due to the higher sensitivity of V_s to the presence of fluids, low V_p/V_s val-
 183 ues are commonly used to indicate low fluid content, and vice versa (Christensen, 1996;
 184 Ito et al., 1979; Eberhart-Phillips et al., 1989, 2005; Audet et al., 2009). For a Poisson
 185 solid (Poisson’s ratio= 0.25), the V_p/V_s ratio is equal to 1.73: we use the Poisson’s solid
 186 as our reference to define high (> 1.73) and low (< 1.73) V_p/V_s ratios. The two high-
 187 velocity anomalies are characterized by low V_p/V_s values (< 1.6) surrounded by higher
 188 V_p/V_s (> 1.8; Figure 4), suggesting lower fluid content compared to the surrounding ac-
 189 cretionary prism. The offshore low-velocity zone is more marked, appearing as a high-
 190 V_p/V_s feature (> 2) adjacent to the Pōrangahau anomaly and coincident with a region
 191 of frequent (every 4–5 years) slow slip events (Figure 2; Wallace, 2020). This high- V_p/V_s
 192 feature is columnar in shape, extending through the entire 30 km depth range illustrated,
 193 suggesting that it may be associated with a source in the subducted oceanic crust.

194 4.2 Resolution analysis

195 Point spread functions (PSFs) provide a measure of how point-like perturbations
 196 are blurred or smeared by an inversion (Fichtner & Trampert, 2011), and have seen ex-
 197 tensive use as resolution tests in adjoint tomography studies (e.g Zhu et al., 2015; Bozdağ
 198 et al., 2016; Tao et al., 2018). To perform point spread tests, we perturb our final ve-
 199 locity model \mathbf{m} by a quantity $\delta\mathbf{m}$, and attempt to recover the perturbation by solving
 200 for the action of the Hessian on the model perturbation (Fichtner & Trampert, 2011).
 201 In practice, this is accomplished using finite-differences of gradients

$$202 \mathbf{H}(\mathbf{m})\delta\mathbf{m} \approx \mathbf{g}(\mathbf{m} + \delta\mathbf{m}) - \mathbf{g}(\mathbf{m}), \quad (1)$$

203 where $\mathbf{H}(\mathbf{m})$ is the Hessian evaluated at the final model \mathbf{m} , $\mathbf{g}(\mathbf{m})$ is the gradient eval-
 204 uated at the final model, and $\delta\mathbf{m}$ is a local model perturbation with respect to the fi-
 205 nal model. The resulting quantity $\mathbf{H}(\mathbf{m})\delta\mathbf{m}$ is a conservative estimate of the PSF, which
 206 provides practical information on the extent of how features in the tomographic model
 207 can be interpreted (Fichtner & Trampert, 2011). Individual point spread tests define $\delta\mathbf{m}$
 208 as a 3D spheroidal Gaussian with peak amplitude equal to 15% of the final V_s model.
 209 The size and location of the perturbations are chosen to reflect the individual velocity
 210 anomaly being probed. We perform four individual point spread tests to understand the
 resolution of the anomalies identified in Section 4.1.

211 In Chow et al. (companion manuscript) we also calculate the Fourier transform of
 212 the Hessian at zero wavenumber, or zeroth moment, which conveys how resolution of the
 213 underlying dataset varies across the model domain. The zeroth moment test recovers a

homogeneous volumetric perturbation in place of $\delta\mathbf{m}$ (Fichtner & Trampert, 2011). In similar fashion to a ray coverage plot, the zeroth moment shows how resolution varies relatively, but does not provide information on resolution length. Depth slices through the zeroth moment volume are shown in Figure A1, using a threshold value chosen to represent the lateral extent of sensitivity in our velocity model. The threshold region contains all three velocity anomalies to depths of 25 km, meaning our dataset is sensitive to velocity heterogeneities in these regions. The pink shaded areas in Figures 3 and 4 show the same threshold value in which the updated velocity model is interpretable.

The PSF for the Māhia Peninsula anomaly has a complicated geometry (Feature M; Figure 5A, C). The peak of the PSF lies a few kilometers offshore from the perturbation itself, indicating uncertainty of a few kilometers in deriving an exact location (Figure 5A). Similarly, lateral smearing over ~ 100 km suggests that the size of the heterogeneity is not well constrained and that the actual heterogeneity could be smaller than the corresponding velocity signature. Interestingly, the PSF contains a second peak further inland, and a high-amplitude feature to the south, indicating that the updated velocity structure at these locations is affected by heterogeneity beneath the Peninsula. The model shows no corresponding high-velocity anomalies at these locations however (Figure 3), suggesting that this trade-off does not significantly impact the final velocity model. Vertical smearing (Figure 5C) indicates that the heterogeneity affects the inferred velocity structure above and below itself, which likely explains the large vertical extent seen in the V_s and V_p/V_s models (Figures 3, 4).

The PSF for the Pōrangahau anomaly (Feature P; Figure 4) shows that the heterogeneity here is more well-resolved, with location uncertainty of a few kilometers (Figure 5B). The PSF also indicates that there is minimal trade-off with the surrounding velocity structure, but lateral smearing means that the width of the velocity anomaly may be larger than the actual heterogeneity. In cross-section (Figure 5D), the peak of the PSF is located a few kilometers above the input perturbation. This may explain the apparent shallow, mid-crastal depth of the Pōrangahau anomaly (Figure 4C), which may be an artefact of the inversion. Conversely, this suggests that the true heterogeneity is likely situated deeper than the corresponding velocity anomaly, and that the shallow, vertically-elongated velocity structure is a result of vertical smearing (Figure 5D).

We perform two additional point spread tests to assess the resolution of the offshore low-velocity anomaly (Feature O; Figure 4). The first test attempts to recover a low-velocity anomaly within the subducting slab (Figure 5E). The resulting PSF shows a columnar structure, similar to that observed in V_p/V_s (Figure 4C). To ensure that this columnar structure could not also be the result of a velocity anomaly in the upper plate, we perform a similar test for a low-velocity anomaly input above the plate interface (Figure 5F). The resulting PSF shows that recovery is primarily confined to the upper plate, and consequently implies that the presence of an upper-plate, low-velocity feature would not explain the offshore low-velocity anomaly imaged. In other words, the heterogeneity (Feature O; Figure 4) is likely an intra-slab low-velocity ($\text{high-}V_p/V_s$) anomaly, whose signature is smeared considerably in the vertical direction (Figure 4C).

Overall, the point spread tests performed for the East Coast velocity anomalies suggest that: (1) the lateral locations of the anomalies are well resolved, with spatial uncertainties less than ten kilometers; (2) the lateral extent of the features is affected by smearing, but may be roughly estimated by measuring the width of the peak amplitudes of the velocity anomalies; and (3) the vertical extent and exact depths of the features are not well-constrained but the two high-velocity anomalies are likely at interface depths and the low-velocity and high- V_p/V_s offshore anomaly is located within the subducting slab.

264 **4.3 Isosurface visualization**

265 Isosurfaces represent points of constant value within a volume of space and are a
 266 useful tool for highlighting structures within three-dimensional models. To better visu-
 267 alize the high-velocity anomalies below the East Coast we investigated various velocity
 268 isosurfaces using our V_s velocity model. The selected isosurface defines a constant $V_s=3$ km/s
 269 with vertically exaggerated points colored by depth (Figure 6A). The isosurface is ro-
 270 tated to an oblique, trench-perpendicular viewing angle so that both velocity anomalies
 271 are clearly visible.

272 We choose the value of the isosurface ($V_s=3$ km/s) to highlight the most promi-
 273 nent segments of the high-velocity anomalies discussed previously, identifiable as yellow
 274 colors in Figure 3B–D. In terms of tectonic structure, this process can be thought of as
 275 the stripping away of low-velocity sediments overlying stiffer material such as oceanic
 276 and continental crust. This effect is clearly visible in the isosurface as removal of the sed-
 277 imimentary and volcanic cover on the Australian plate and the adjacent accretionary wedge
 278 (Figure 6A; Edbrooke et al., 2015). The remaining structures are likely related to base-
 279 ment rocks of the North and South Islands (Mortimer, 2004) and the backstop of the sub-
 280 duction zone forearc (Byrne et al., 1993).

281 Clearly identifiable in the isosurface are two solitary peaks related to the high-velocity
 282 anomalies below Pōrangahau and Māhia Peninsula. Similar to the 2D cross-sections (Fig-
 283 ure 3B–D), the Pōrangahau anomaly is a tall, narrow peak that extends to the surface,
 284 while the Māhia Peninsula anomaly features a wide base and lower relative height. Fur-
 285 ther seaward a third prominent peak is visible, which spatially correlates with Rock Gar-
 286 den, a known seamount on the incoming Pacific plate (Barnes et al., 2010). Other sec-
 287 tions of the isosurface can be linked to known tectonic features of New Zealand. These
 288 include a notch in the backstop related to Cook Strait (K. B. Lewis et al., 1994), deep
 289 depressions related to Taranaki basin (e.g., King & Thrasher, 1996) and Whanganui basin
 290 (e.g., Carter & Naish, 1998), and a collection of shallow depressions throughout the Taupō
 291 Volcanic Zone (Wilson et al., 1995, 2009). These tectonic features are discussed in more
 292 detail in Chow et al. (companion manuscript).

293 **5 Discussion**294 **5.1 Deeply subducted seamounts below the East Coast**

295 We interpret the East Coast high-velocity anomalies as previously-unidentified deeply-
 296 subducted seamounts located below Pōrangahau and Māhia Peninsula (Figure 1). The
 297 3 km/s isosurface of the velocity model highlights these features, and their apparent ef-
 298 fect on the velocity structure of the upper crust, remarkably well (Figure 6A). We can
 299 estimate the size and depth of the two seamounts, but note that depending on their ac-
 300 tual shape and aspect ratio their full extent may fall below the resolution limit of the
 301 tomographic inversion. In other words, the lateral width of the seamounts could be larger
 302 than the corresponding velocity signature.

303 Subduction of partially buried seamounts would have an observable effect on the
 304 structure of the accretionary prism and the upper plate, which can be corroborated with
 305 known geologic features. Sand table experiments and field observations have been used
 306 to predict the effects of subducted seamounts on the upper plate, which include: tectonic
 307 erosion at the frontal wedge leading to re-entrant bathymetric features, a complex frac-
 308 ture network that forms in the vicinity of the seamount and is preserved as a permanent
 309 furrow or scar, local uplift above the seamount, and increased subsidence in the seamount's
 310 wake (Figure 6B; Dominguez et al., 1998, 2000).

311 **5.1.1 Māhia Peninsula seamount**

312 We propose that a large seamount has been subducted below Māhia Peninsula. We
 313 estimate the extent of this Māhia Peninsula seamount at 25 km based on its V_p/V_s sig-
 314 nature. A seamount attached to the incoming plate would sit at plate interface depth,
 315 which is at approximately 12 km depth (Williams et al., 2013). In this section we present
 316 external evidence that corroborates our interpretation.

317 The Poverty Re-entrant northeast of Māhia Peninsula has been interpreted as a
 318 seamount scar resulting from consecutive seamount impacts over the last 1–2 Myr (Figure 6C;
 319 K. Lewis & Pettinga, 1993; Collot et al., 1996; K. B. Lewis et al., 1998; Pedley et al.,
 320 2010). Based on relative locations and the plate convergence direction, it is likely this
 321 re-entrant is associated with the Māhia Peninsula seamount. The Poverty Re-entrant
 322 has previously been identified as a double feature consisting of lower and upper inden-
 323 tations (Collot et al., 1996). The geometry of the lower indentation (i.e. steep-sided, “V”-
 324 shaped deflection of the frontal wedge) is suggestive of a re-entrant, while the morphol-
 325 ogy of the upper indentation indicates eastward subsidence and subsequent canyon ero-
 326 sion (Collot et al., 1996). The upper Poverty indentation has been linked to subsidence
 327 and drainage development in the wake of a very large seamount (Pedley et al., 2010),
 328 which we propose may be the Māhia Peninsula seamount imaged here. Topographic up-
 329 lift would similarly be expected for a seamount below land, and may explain the anom-
 330 lous topographic high of Māhia Peninsula with respect to the surrounding coastline (Fig-
 331 ure 6C).

332 Other studies have inferred the presence of a deeply subducted seamount near Māhia
 333 Peninsula. The offshore Lachlan fault system (Figure 1) has undergone almost 6 km ver-
 334 tical separation of its northern segment with respect to its southern extent, which Barnes
 335 et al. (2002) hypothesized to be the upper-plate response to a subducted seamount >10 km
 336 below the Peninsula. Approximately 20 km landward of Māhia Peninsula, the Mōrere
 337 thermal spring is one of only two thermal springs in this region, whose chemical signa-
 338 ture show enrichment in mantle components suggesting that high-permeability paths ex-
 339 tend from the subducted plate to the surface (Figure 1; Reyes et al., 2010). The coinci-
 340 dent Mōrere magnetic anomaly has been linked to a seamount subducted within the
 341 last 2 Myr (+70 nT; Hunt & Glover, 1995), which agrees with previous associations of
 342 positive magnetic anomalies with locations of offshore seamounts (Bell et al., 2010).

343 Below the Mōrere thermal spring, ray-based tomography revealed a high- V_p anomaly
 344 at approximately 8 km depth, which was suggested to be volcanic in origin (Eberhart-
 345 Phillips et al., 2015). Magnetotelluric studies here show a conductive patch on the plate
 346 interface, with a more resistive patch below the Peninsula (Heise et al., 2017). The con-
 347 ductive patch was interpreted to indicate the presence of fluid- or clay-rich sediments,
 348 and may be related to underthrust, fluid rich sediments at the leading flank of the seamount,
 349 similar to those proposed for offshore seamounts at the northern Hikurangi margin (Bell
 350 et al., 2010). The Mōrere anomalies may thus correspond to the down-dip extent of the
 351 seamount below Māhia Peninsula, as well as the upper crust response to such a geomet-
 352 ric heterogeneity.

353 **5.1.2 Pōrangahau seamount**

354 We propose that a previously unrecognised seamount has been subducted almost
 355 100 km beyond the trench and now lies below the East Coast township of Pōrangahau.
 356 From the V_p/V_s signature (Figure 4) this inferred Pōrangahau seamount has an approx-
 357 imate lateral extent of 15 km. The seamount is inferred to lie at a plate interface depth
 358 of 15 km (Williams et al., 2013).

359 A distinctive bathymetric feature in the vicinity of the Pōrangahau seamount is
 360 Madden Canyon. Although it is too far from the trench (~ 100 km) to be easily explained

361 as a re-entrant, Madden Canyon may have formed as an area of subsidence in which mass
 362 sliding and canyon erosion was promoted at the trailing flank of the Pōrangahau seamount
 363 (Figure 6C; Dominguez et al., 1998). There is no obvious re-entrant feature in the bathymetry
 364 data related to the Pōrangahau seamount (Figure 6C), but rapid growth of the accre-
 365 tionary pile at the central Hikurangi margin may have obscured such a feature (Von Huene
 366 & Scholl, 1991). Similarly, there is no corresponding topographic high, like that repre-
 367 sented by Māhia Peninsula, which may indicate that the Pōrangahau seamount lies at
 368 a deeper interface depth or is smaller (or both) than the Māhia Peninsula seamount.

369 Evidence corroborating the presence of the Pōrangahau seamount is limited, which
 370 may in part reflect a lack of targeted geophysical studies in this region. The contrast in
 371 evidence between the Pōrangahau and Māhia Peninsula seamounts could also be explained
 372 by the ages of the two seamounts. A back-of-the-envelope calculation based on a mar-
 373 gin normal convergence rate of 39 mm/yr (Figure 2; Wallace, 2020) and distance to the
 374 trench of 150 km (Figure 1), suggests that the Pōrangahau seamount first impacted the
 375 trench at \sim 4 Ma. In contrast, the Māhia Peninsula seamount is thought to have sub-
 376 ducted in the last 1–2 Myr (K. B. Lewis et al., 1998; Pedley et al., 2010). This differ-
 377 ence may explain the contrast in the velocity signatures of the two seamounts. Other po-
 378 tentially impactful differences between the two inferred seamounts that are not well con-
 379 strained by our results include: the differing characteristics of the accretionary prism,
 380 the size and aspect ratio of each seamount, and their respective burial depths prior to
 381 subduction.

382 5.2 Implications for seismic and aseismic behavior

383 Seamounts entering the Hikurangi subduction zone have previously been identi-
 384 fied in the early stages of subduction. Recognition of the Māhia and Pōrangahau sub-
 385 ducted seamounts in this study may help to explain anomalous seismic and aseismic be-
 386 havior observed up-dip from their respective locations. Mentioned previously, numerous
 387 factors have been suggested as explanations for variations in coupling coefficient on the
 388 Hikurangi megathrust interface. One such interpretation suggests that permeability vari-
 389 ations in North Island terrane blocks results in heterogeneous fluid distribution on the
 390 interface, leading to the variations in plate coupling (Reyners et al., 2017). However based
 391 on our findings, we suggest that the inferred seamounts at Mahia Peninsula and Pōrangahau
 392 may play a more central role in along-strike variations in plate coupling.

393 A study that used finite element modeling of seamount subduction suggests that
 394 sediment overconsolidation on the leading flanks of seamounts results in fracturing of the
 395 upper plate and increased tectonic compression and yield strength, favoring the storage
 396 of elastic strain and seismic behavior (Sun et al., 2020). In contrast, underconsolidation
 397 in the stress shadow of the seamount is predicted to result in increased porosity, decreased
 398 tectonic compression, and a preference for aseismic behavior such as slow slip (Figure 7B).

399 Pōrangahau and Māhia Peninsula are both areas of anomalously high rates of clus-
 400 tered seismicity, which may be manifestations of small-to-moderate sized earthquakes
 401 observed at the leading edge of subducted seamounts (Bell et al., 2010). Pōrangahau has
 402 seen repeated episodes of moderate-magnitude swarm seismicity (Jacobs et al., 2016),
 403 and moderately sized earthquakes accompanying geodetically observed SSEs (Figure 7C;
 404 Wallace, Beavan, et al., 2012). At Māhia Peninsula, triggered microseismicity has been
 405 temporally correlated with shallow SSEs in the region, clustered near the Peninsula (Figure 7D;
 406 Delahaye et al., 2009). The increased seismic activity at these two locations may be linked
 407 to the inferred seamounts, but further work is needed to draw connections between fault-
 408 ing mechanisms, earthquake depth, and inferred seamount locations.

409 Geodetic observations show that the locked-to-creeping transition on the Hikurangi
 410 plate interface extends approximately NW–SE through the central Hikurangi margin,
 411 perpendicular to the trench axis and almost directly through Pōrangahau (Figure 2; Wal-

lace, 2020). The margin further south is interpreted to be more geometrically and compositionally uniform, enabling broader zones of locking, while to the north shallow slow slip events accommodate a majority of plate motion aseismically (Wallace, 2020). Interestingly, the spatial extent of the shallow northern SSEs is segmented around Hawke Bay, with a southern terminus just south of Pōrangahau (Figure 7A). This segmentation roughly correlates with the locations of the two deeply subducted seamounts and may be linked to the affected upper-plate regions surrounding each seamount (dashed blue circles; Figure 2).

Several theories have been posited to link seamounts with megathrust slip behavior. Based on the locations of our two seamounts in a predominantly aseismic patch of the plate interface (Figure 2), our findings are consistent with the idea put forth by Wang and Bilek (2011) that describes seamounts as geometric irregularities impinging on the upper plate. According to this interpretation, seamounts must break through upper plate rocks to accommodate plate convergence and, at low temperatures corresponding to shallow seismogenic depths, this results in fracturing of the accretionary wedge and upper plate, and to a lesser degree the seamount itself. Between the point at which a seamount initially enters the trench and the depths at which mantle viscosity becomes relevant, these seamounts are expected to damage their surroundings brittlely, leaving a permanent scar in their wake that is less able to accumulate elastic strain necessary for coseismic rupture propagation (Wang & Bilek, 2011; Cummins et al., 2002; Bangs et al., 2006).

We propose that repeated seamount subduction at the northern Hikurangi margin has resulted in a region of extensive upper plate fracturing (Figure 7A). In contrast, any seamounts entering the southern margin are thought to be buried under several kilometers of sediments, which may suppress their effects on upper plate morphology and allow the interface to lock (Figure 7B; Wallace, 2020). This line of argument has previously been unable to account for the location of the locked-to-creeping transition at the central Hikurangi margin, because the central margin features a more well-developed accretionary wedge with respect to the northern margin. This is more consistent with a smooth incoming seafloor and therefore a locked interface (Wallace, 2020), but our recognition of a seamount below Pōrangahau is capable of explaining the location of the locked-to-creeping transition. In other words, the seamount at Pōrangahau may represent the southern extent of partially buried seamounts that are able to significantly influence the mechanical integrity of the upper plate.

The high- V_p/V_s intraslab feature (Figure 4C) identified in this study may also play a role in SSE timing and location. Warren-Smith et al. (2019) proposed that episodic release of fluid pressure from the over pressured subducting crust into the upper plate influences the timing of slow slip events on the megathrust. Our imaged high- V_p/V_s anomaly may be a manifestation of fluids in the subducting slab, and its location below the southern end of a region of repeating SSEs (Figure 7D) appears to agree with the idea that accumulation and release of fluid pressure has an influence on slow slip events (Warren-Smith et al., 2019). The proximity of the inferred fluid source to the Pōrangahau seamount also suggests some link. Seamount subduction modeling suggests that aseismic slip should be the preferred behavior at the trailing flank of a subducted seamount (Figure 7B; Sun et al., 2020), but further work is needed to draw firm connections between fluids in the downgoing slab, shallow slow slip events, and subducted seamounts.

6 Conclusions

We identify velocity anomalies below the east coast of the North Island of New Zealand using a newly-derived adjoint tomography velocity model. Point spread functions are used to constrain the robustness of these features, showing that they are well resolved, although smearing in the inversion procedure increases the uncertainty of their sizes and shapes.

The two high-velocity anomalies are interpreted as previously-unidentified, deeply-subducted seamounts below Māhia Peninsula and Pōrangahau, and a distinctive low-velocity (high- V_p/V_s) anomaly corresponding to an intraslab fluid source. The approximate size and location of the two seamounts are consistent with those of known offshore seamounts, and with the existence of bathymetric features predicted by analog sand table experiments. We propose the Poverty Re-entrant to be both the re-entrant and associated subsidence feature related to subduction of the Māhia Peninsula seamount. The anomalous topographic high of the Peninsula is also linked to predicted topographic uplift above the inferred seamount. We propose that Madden Canyon is a corresponding subsidence feature related to the Pōrangahau seamount, which first impacted the trench ~ 4 Ma, based on modern plate convergence rates. We suggest that corresponding evidence such as a re-entrant or topographic uplift may be obscured due to the relative age, size, or location of the seamount relative to the Māhia Peninsula seamount.

Anomalous seismic and geodetic phenomena observed at Pōrangahau and Māhia Peninsula — including swarm seismicity, magnetic anomalies, and a solitary thermal spring west of Māhia Peninsula — are plausibly explained by the existence of deeply subducted seamounts. Plate coupling and shallow SSEs inferred from geodetic observations and inversions also correlate well with the locations of these seamounts. An inferred intraslab fluid source offshore Pōrangahau is imaged below a region of frequent, shallow SSEs and its location is in agreement with previous ideas linking the release of fluid pressure from the downgoing plate with the timing of SSEs.

Based on these findings, we suggest that the upper plate is left extensively fractured in the wake of each subducting seamount, making it less capable than otherwise of storing elastic strain. We propose that upper plate damage can account for the observed differences in along-strike properties of the Hikurangi subduction zone, provides a possible explanation for the locked-to-creeping transition zone and segmentation of shallow SSEs observed, and may mitigate the extent and effects of future large subduction zone earthquakes.

Open Research

The adjoint tomography velocity model analyzed in this study is available through a public repository (<https://core.geo.vuw.ac.nz/d/feae69f61ea54f81bee1/>). References to data used to derive this velocity model can be found in the following intext citation reference: Chow et al. (companion manuscript).

The authors are in the process of archiving the velocity model on the more permanent public repository: the Incorporated Research Institutions for Seismology Earth Model Collaboration (IRIS EMC).

Acknowledgments

This work was funded by a Rutherford Discovery Fellowship and Marsden Fund awarded by the Royal Society of New Zealand, as well as an Endeavour Fund awarded by the New Zealand Ministry of Business, Innovation and Employment. We thank Laura Wallace, Susan Ellis, and Phil Barnes for helpful discussions.

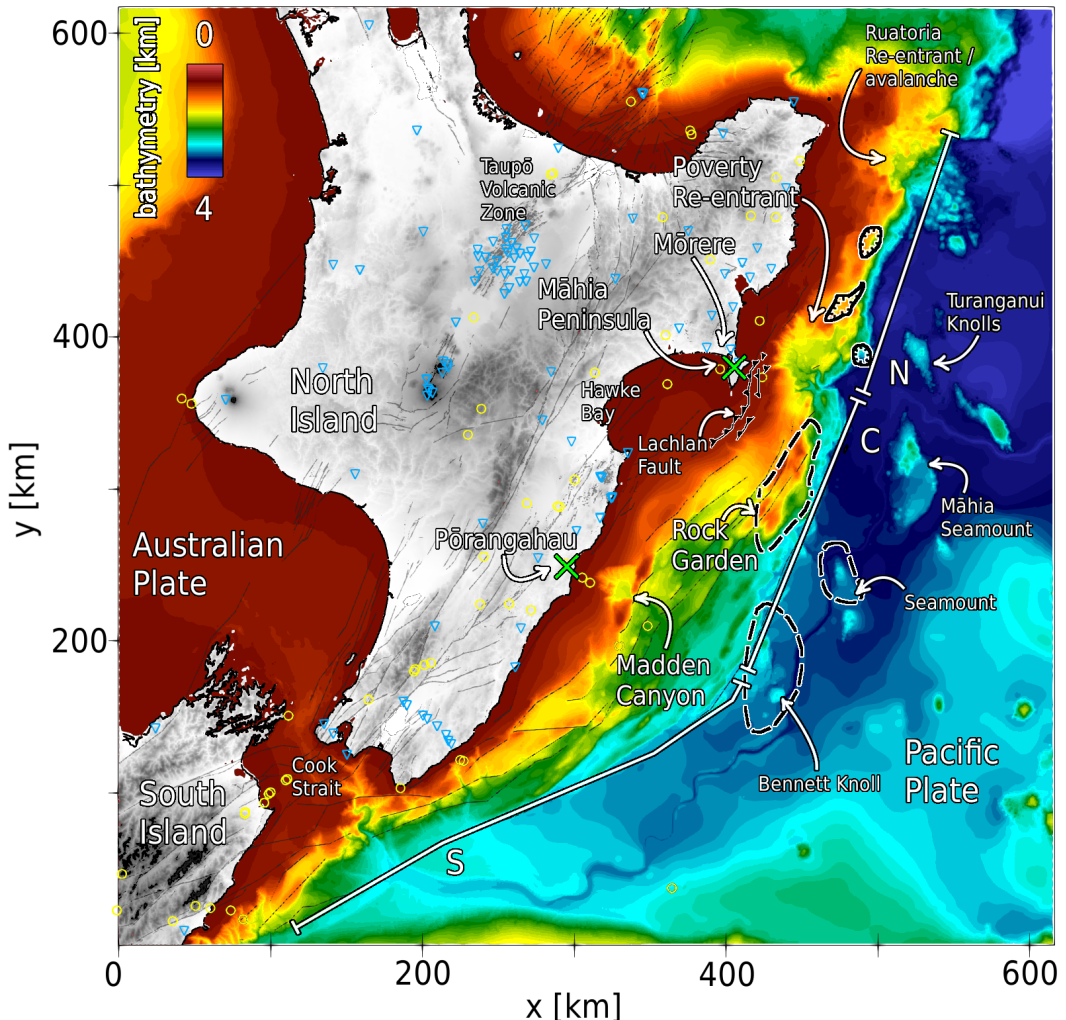


Figure 1. Tectonic setting for the Hikurangi subduction zone offshore New Zealand’s North Island. High-resolution bathymetry (Mitchell et al., 2012) highlights the complicated accretionary wedge and numerous seamounts on the incoming Pacific Plate. White solid lines separate the margin into southern (S), central (C), and northern (N) segments. Green crosses show the locations of velocity anomalies below Pōrangahau and Māhia Peninsula. Yellow circles and blue inverted triangles show earthquakes and receivers used to derive the velocity model (Chow et al., companion manuscript). Thin black lines show active faults (Litchfield et al., 2014). Seamounts identified in previous studies are shown with dashed black outlines (Barnes et al., 2010) and solid black outlines (Bell et al., 2010).

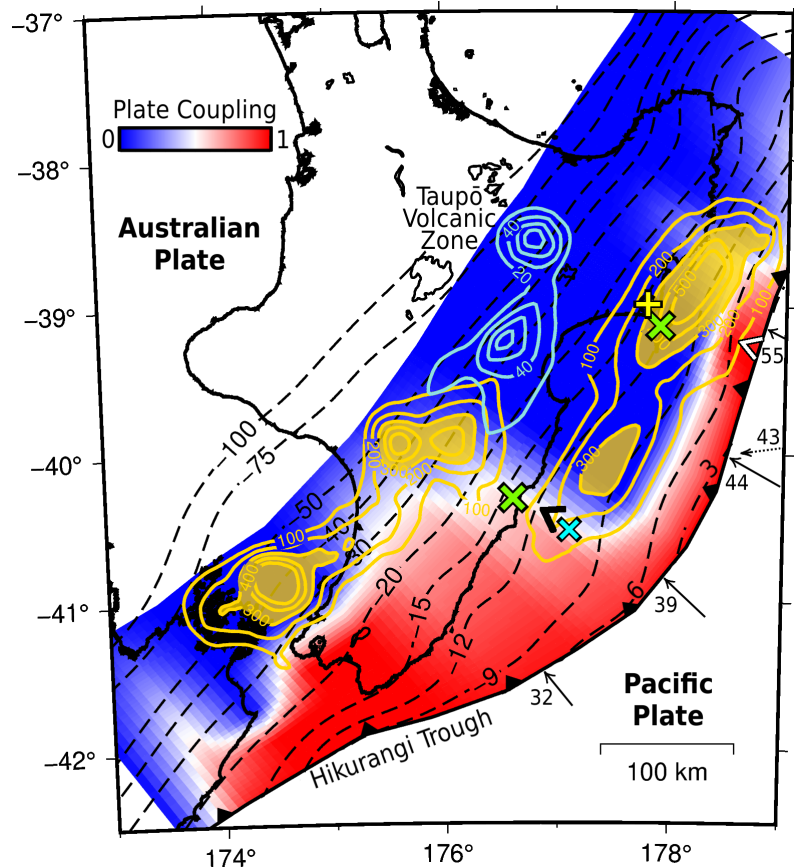


Figure 2. Geophysical setting of the Hikurangi subduction zone. Arrows denote trench-normal convergence rate in units of mm/yr. The dashed arrow shows the plate convergence direction and rate. Colors representing plate coupling coefficient show that the southern Hikurangi margin is effectively locked to 30 km depth (Wallace, Barnes, et al., 2012). Cumulative slow slip events from 2002–2014 shown as yellow and blue contours in units of millimeters. Shaded patches highlight cumulative slip greater than 300 mm. Green X’s represent inferred deeply-subducted seamounts. The blue X shows the location of an inferred fluid source in the subducting slab. Black and white “<” markers represent the approximate locations of Madden Canyon and Poverty Re-entrant, respectively. Yellow “+” shows the location of the Mōrere thermal spring, and corresponding geophysical anomalies. Dashed black lines show depth to the plate interface in units of kilometers (Williams et al., 2013).

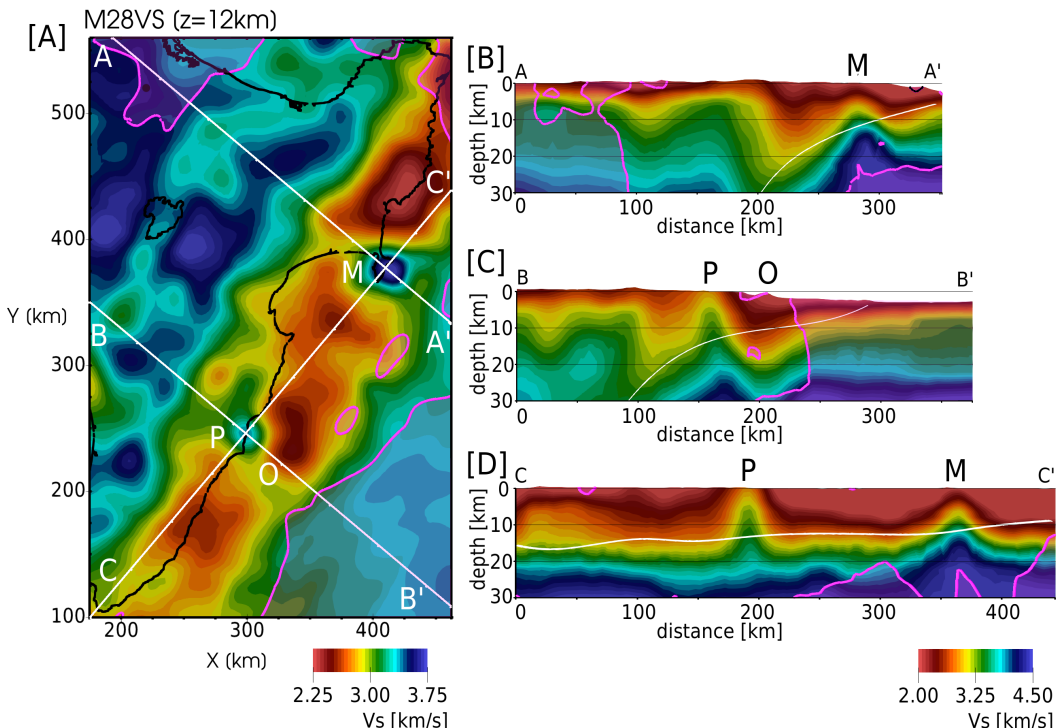


Figure 3. East Coast velocity anomalies shown in V_s . Pink shaded regions highlight the model domain outside the chosen sensitivity threshold, within which model parameters are not interpreted (Figure A1). A) V_s at 12 km depth showing two localized high-velocity anomalies below Pōrangahau (P) and Māhia Peninsula (M), and a broad low-velocity anomaly offshore Pōrangahau (O). Surface traces of cross sections are shown as white lines. B–D) Cross sections through velocity anomalies corresponding to the surface traces shown in A at 3 \times vertical exaggeration. White line shows plate interface model of Williams et al. (2013).

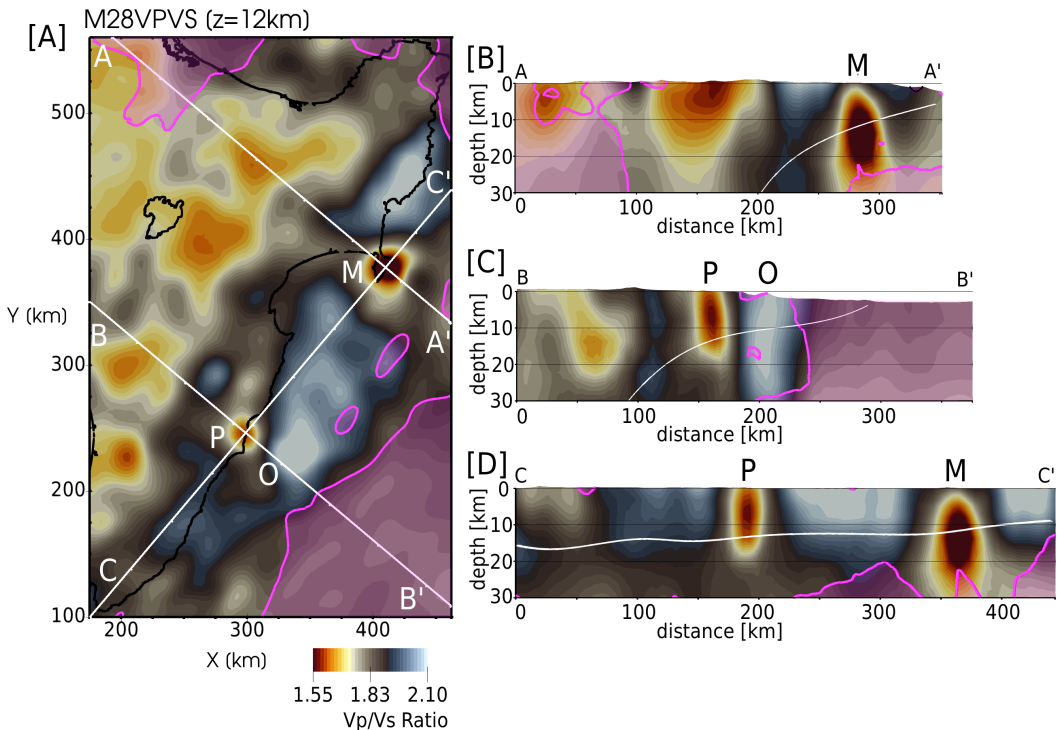


Figure 4. East Coast velocity anomalies in V_p/V_s . Pink shaded regions highlight the model domain outside the chosen sensitivity threshold, within which model parameters are not interpreted (Figure A1). A) V_p/V_s at 12 km depth showing two localized low- V_p/V_s anomalies below Pōrangahau (P) and Māhia Peninsula (M), and a broad high- V_p/V_s anomaly offshore Pōrangahau (O). Surface traces of cross sections are shown as white lines. B–D) Cross sections through high-velocity anomalies corresponding to the surface traces shown in A at 3× vertical exaggeration. White line shows plate interface model of Williams et al. (2013).

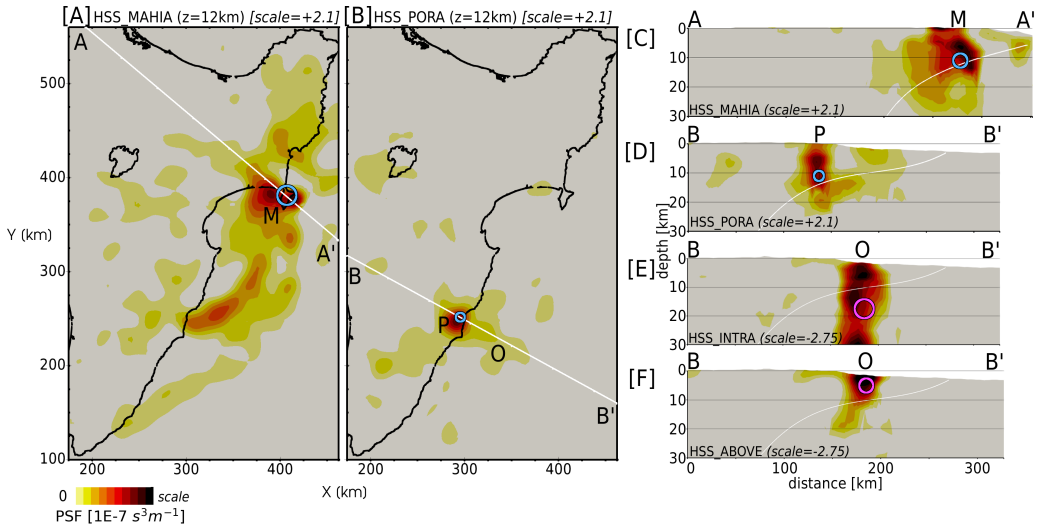


Figure 5. Point spread functions (PSFs) for the Māhia Peninsula (M), Pōrangahau (P), and offshore (O) velocity anomalies. Input perturbations are 3D spheroidal Gaussians with peak amplitudes equal to $\pm 15\%$ of the background V_s model. Horizontal (Γ_h) and vertical (Γ_z) full width of the Gaussian perturbations are shown as blue circles for positive perturbations, and pink circles for negative perturbations. A) Māhia Peninsula PSF ($\Gamma_h = 20$ km); A–A' trace shown in panel C. B) Pōrangahau PSF ($\Gamma_h = 10$ km); B–B' trace shown in panels D–F. C) Māhia Peninsula PSF A–A' cross section ($\Gamma_z = 5$ km). D) Pōrangahau PSF B–B' cross section ($\Gamma_z = 3.5$ km). E) Intra slab low-velocity anomaly PSF ($\Gamma_{h,z} = 21, 7$ km). F) Above slab low-velocity anomaly PSF ($\Gamma_{h,z} = 15, 5$ km). Note the varying amplitude scale. Cross sections shown at $3\times$ vertical exaggeration. White line in cross sections shows plate interface model of Williams et al. (2013).

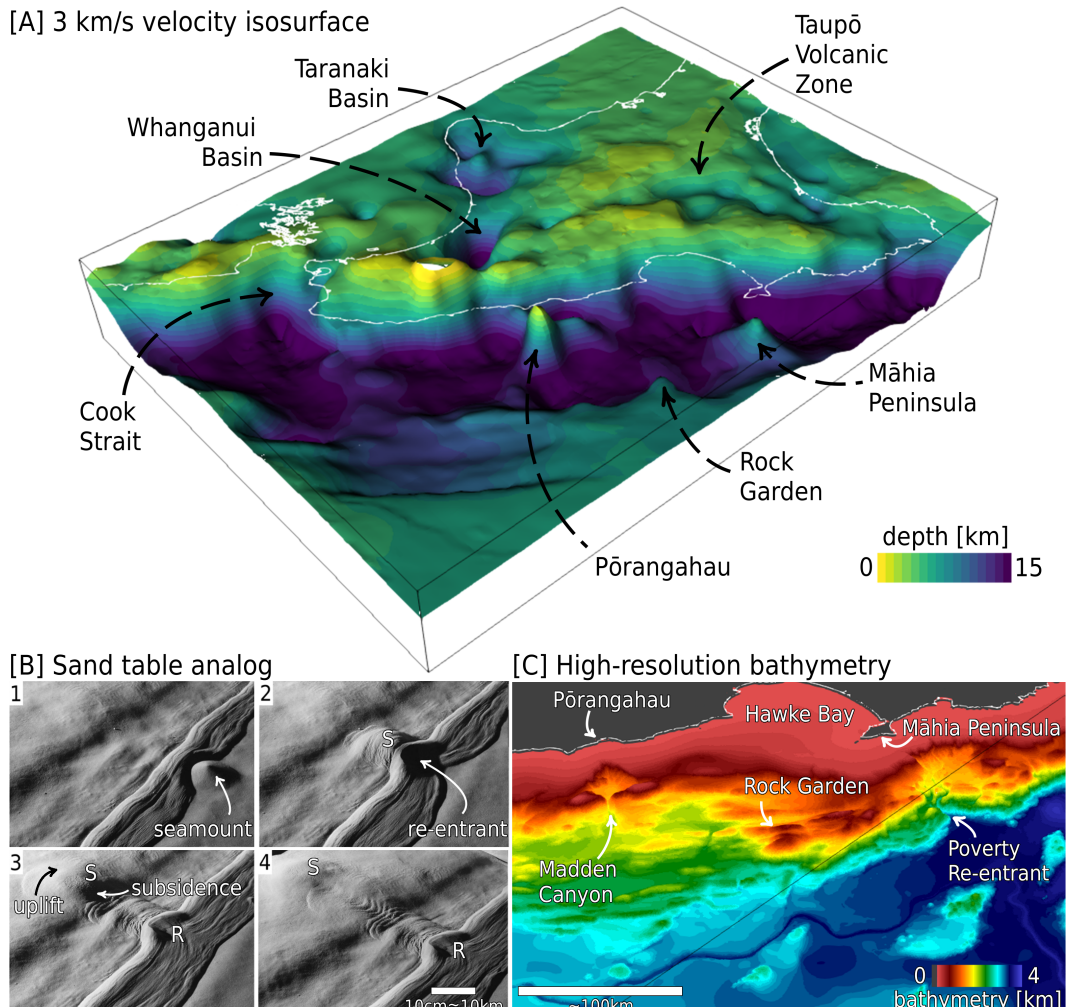


Figure 6. Evidence for deeply subducted seamounts below the East Coast. A) Isosurface for $V_s=3$ km/s colored by depth and vertically exaggerated. Anomalies related to the two inferred seamounts below Pōrangahau and Māhia Peninsula are visible as peaks that likely represent expressions of the seamounts on the upper plate. Also visible is a peaked anomaly related to the known seamount at Rock Garden (C). B) Seamount subduction represented by an analog sand table experiment, modified from Dominguez et al. (1998). Panels represent increasing time: B1) The seamount (S) indents the inner trench slope; B2) A shadow zone forms in the wake of the seamount. The re-entrant (R) is affected by intense mass-sliding; B3) The seamount is subducted further, with local uplift above the seamount, and subsidence in its wake; B4) Extension occurs in the wake of the seamount, leading to a subsided area behind the crest of the seamount. A permanent fracture network is left in the upper plate. C) Offshore East Coast bathymetry showing the relative locations of inferred seamounts and bathymetric features (Mitchell et al., 2012).

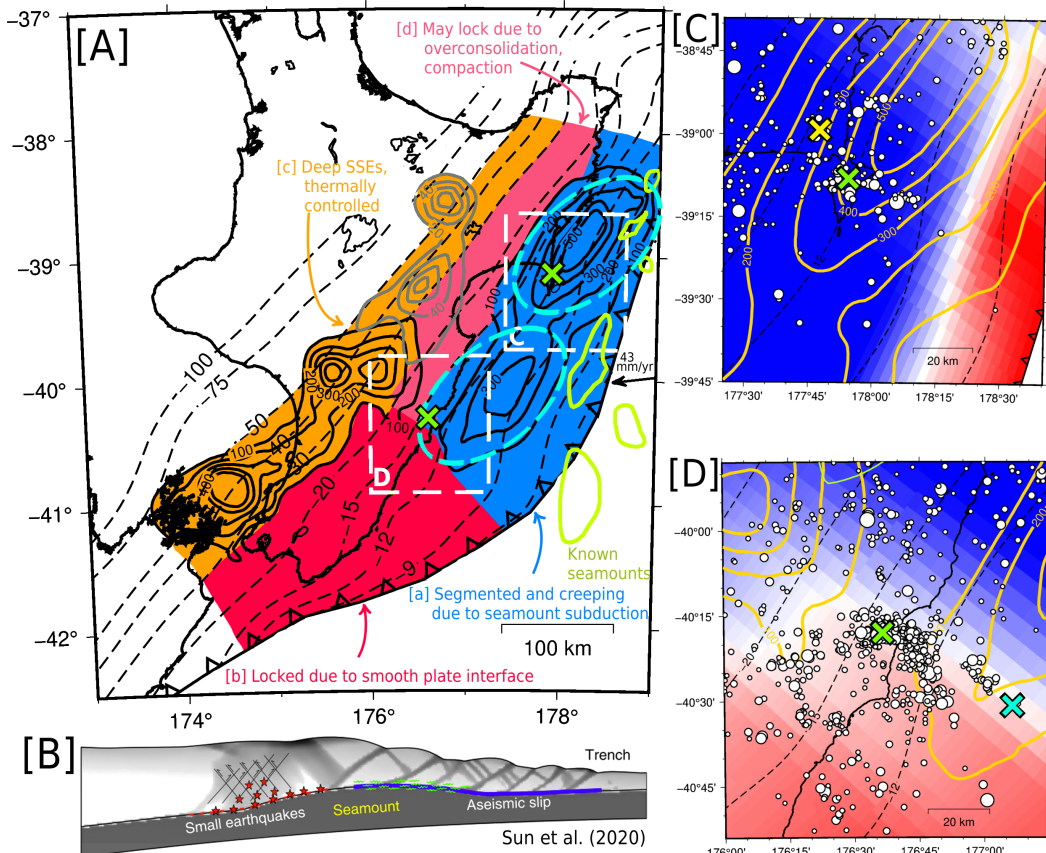


Figure 7. Subducted seamounts (green X's) and seismic and aseismic behavior observed at the Hikurangi subduction margin. A) Possible segmentation of the plate interface, controlled by rough crust subduction at the northern and central Hikurangi margins, in contrast to smooth plate interface at the southern margin. Spatial segmentation of shallow slow slip events highlighted by blue dashed ovals. B) Cartoon cross section of a subduction zone showing expected slip behavior and upper plate faulting during seamount subduction from Sun et al. (2020). C) Māhia Peninsula seamount seismic and aseismic behavior. Earthquakes between 2000 and 2021, $M > 2.5$ at 1 km below or 4 km above plate interface depths (Williams et al., 2013) shown as white circles. Mōrere thermal spring shown as yellow X. D) Pōrangahau seamount seismic and aseismic behavior. Blue cross shows location of inferred intraslab fluids.

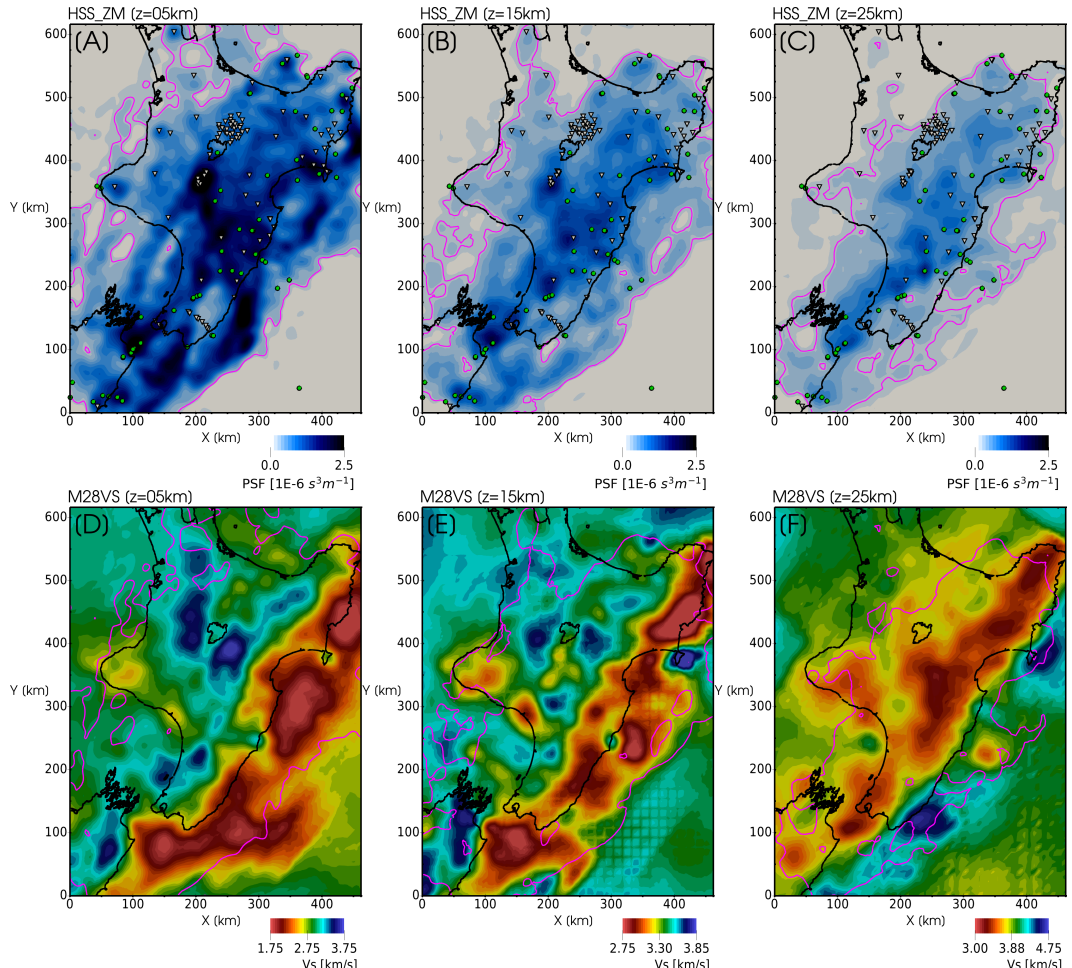


Figure A1. Zeroth moment point spread function (PSF) defining spatial sensitivity of the dataset used to derive our velocity model. The pink line corresponds to a threshold value of $2 \times 10^{-7} \text{ s}^3 \text{ m}^{-1}$. Velocity heterogeneities located in regions below the threshold have limited to no sensitivity and are consequently not interpreted. A–C) Depth slices through the zeroth moment PSF at 5, 15, and 25 km depth. Green circles and inverted triangles denote sources and receivers used in the inversion, respectively. D–E) Depth slices through our V_s velocity model at 5, 15, and 25 km depth. Pink lines are the same as those shown in A–C.

503 **References**

- Audet, P., Bostock, M. G., Christensen, N. I., & Peacock, S. M. (2009). Seismic evidence for overpressured subducted oceanic crust and megathrust fault sealing. *Nature*, 457(7225), 76–78.
- Bangs, N. L., Gulick, S. P., & Shipley, T. H. (2006). Seamount subduction erosion in the Nankai Trough and its potential impact on the seismogenic zone. *Geology*, 34(8), 701–704.
- Barker, D., Sutherland, R., Henrys, S., & Bannister, S. (2009). Geometry of the Hikurangi subduction thrust and upper plate, North Island, New Zealand. *Geochemistry, Geophysics, Geosystems*, 10(2).
- Barnes, P. M., Lamarche, G., Bialas, J., Henrys, S., Pecher, I., Netzeband, G. L., ... Crutchley, G. (2010). Tectonic and geological framework for gas hydrates and cold seeps on the Hikurangi subduction margin, New Zealand. *Marine Geology*, 272(1-4), 26–48.
- Barnes, P. M., Nicol, A., & Harrison, T. (2002). Late Cenozoic evolution and earthquake potential of an active listric thrust complex above the Hikurangi subduction zone, New Zealand. *Geological Society of America Bulletin*, 114(11), 1379–1405.
- Beanland, S., & Haines, J. (1998). The kinematics of active deformation in the North Island, New Zealand, determined from geological strain rates. *New Zealand Journal of Geology and Geophysics*, 41(4), 311–323.
- Bell, R., Sutherland, R., Barker, D., Henrys, S., Bannister, S., Wallace, L., & Beavan, J. (2010). Seismic reflection character of the Hikurangi subduction interface, New Zealand, in the region of repeated Gisborne slow slip events. *Geophysical Journal International*, 180(1), 34–48.
- Bozdag, E., Peter, D., Lefebvre, M., Komatitsch, D., Tromp, J., Hill, J., ... Pugmire, D. (2016). Global adjoint tomography: first-generation model. *Geophysical Journal International*, 207(3), 1739–1766.
- Byrne, D. E., Wang, W.-h., & Davis, D. M. (1993). Mechanical role of backstops in the growth of forearcs. *Tectonics*, 12(1), 123–144.
- Carter, R. M., & Naish, T. R. (1998). A review of Wanganui Basin, New Zealand: global reference section for shallow marine, Plio–Pleistocene (2.5–0 Ma) cyclostratigraphy. *Sedimentary Geology*, 122(1-4), 37–52.
- Chesley, C., Naif, S., Key, K., & Bassett, D. (2021). Fluid-rich subducting topography generates anomalous forearc porosity. *Nature*, 595(7866), 255–260.
- Chow, B., Kaneko, Y., Tape, C., Modrak, R., Mortimer, N., Bannister, S., & Townend, J. (companion manuscript). Strong upper-plate heterogeneity at the Hikurangi subduction margin (North Island, New Zealand) imaged by adjoint tomography. *Journal of Geophysical Research: Solid Earth*.
- Chow, B., Kaneko, Y., Tape, C., Modrak, R., & Townend, J. (2020). An automated workflow for adjoint tomography — waveform misfits and synthetic inversions for the North Island, New Zealand. *Geophysical Journal International*, 223(3), 1461–1480.
- Christensen, N. I. (1996). Poisson's ratio and crustal seismology. *Journal of Geophysical Research: Solid Earth*, 101(B2), 3139–3156.
- Collot, J.-Y., Delteil, J., Lewis, K. B., Davy, B., Lamarche, G., Audru, J.-C., ... others (1996). From oblique subduction to intra-continental transpression: Structures of the southern Kermadec-Hikurangi margin from multibeam bathymetry, side-scan sonar and seismic reflection. *Marine Geophysical Researches*, 18(2), 357–381.
- Cummins, P. R., Baba, T., Kodaira, S., & Kaneda, Y. (2002). The 1946 Nankai earthquake and segmentation of the Nankai Trough. *Physics of the Earth and Planetary Interiors*, 132(1-3), 75–87.
- Delahaye, E., Townend, J., Reyners, M., & Rogers, G. (2009). Microseismicity but no tremor accompanying slow slip in the Hikurangi subduction zone, New

- 558 Zealand. *Earth and Planetary Science Letters*, 277(1-2), 21–28.
- 559 Dominguez, S., Lallemand, S., Malavieille, J., & von Huene, R. (1998). Upper plate
560 deformation associated with seamount subduction. *Tectonophysics*, 293(3-4),
561 207–224.
- 562 Dominguez, S., Malavieille, J., & Lallemand, S. E. (2000). Deformation of accre-
563 tionary wedges in response to seamount subduction: Insights from sandbox
564 experiments. *Tectonics*, 19(1), 182–196.
- 565 Eberhart-Phillips, D., Bannister, S., Reyners, M., & Henrys, S. (2020). *New
566 Zealand Wide model 2.2 seismic velocity and Qs and Qp models for New
567 Zealand [dataset]*. Retrieved from zenodo.org/record/3779523 doi:
568 10.5281/zenodo.3779523
- 569 Eberhart-Phillips, D., Han, D.-H., & Zoback, M. D. (1989). Empirical relation-
570 ships among seismic velocity, effective pressure, porosity, and clay content in
571 sandstone. *Geophysics*, 54(1), 82–89.
- 572 Eberhart-Phillips, D., Reyners, M., & Bannister, S. (2015). A 3D QP attenuation
573 model for all of New Zealand. *Seismological Research Letters*, 86(6), 1655–
574 1663.
- 575 Eberhart-Phillips, D., Reyners, M., Chadwick, M., & Chiu, J.-M. (2005). Crustal
576 heterogeneity and subduction processes: 3-D Vp, Vp/Vs and Q in the south-
577 ern North Island, New Zealand. *Geophysical Journal International*, 162(1),
578 270–288.
- 579 Edbrooke, S., Heron, D., Forsyth, P., & Jongens, R. (2015). *Geological map of New
580 Zealand 1:1 000 000. GNS Science Geological Map 2*.
- 581 Ellis, S., Fagereng, A., Barker, D., Henrys, S., Saffer, D., Wallace, L., ... Harris, R.
582 (2015). Fluid budgets along the northern Hikurangi subduction margin, New
583 Zealand: The effect of a subducting seamount on fluid pressure. *Geophysical
584 Journal International*, 202(1), 277–297.
- 585 Fichtner, A., & Trampert, J. (2011). Resolution analysis in full waveform inversion.
586 *Geophysical Journal International*, 187(3), 1604–1624.
- 587 Frederik, M. C., Gulick, S. P., & Miller, J. J. (2020). Effect on Subduction of
588 Deeply Buried Seamounts Offshore of Kodiak Island. *Tectonics*, 39(7),
589 e2019TC005710.
- 590 Heise, W., Caldwell, T. G., Bannister, S., Bertrand, E., Ogawa, Y., Bennie, S., &
591 Ichihara, H. (2017). Mapping subduction interface coupling using magnetotel-
592 lurics: Hikurangi margin, New Zealand. *Geophysical Research Letters*, 44(18),
593 9261–9266.
- 594 Hunt, T., & Glover, R. (1995). *Origin of mineral springs on the east coast, North Is-
595 land, NZ* (Tech. Rep.). Wairakei Research Centre, IGNS, Taupo, NZ.
- 596 Ito, H., DeVilbiss, J., & Nur, A. (1979). Compressional and shear waves in sat-
597 urated rock during water-steam transition. *Journal of Geophysical Research:
598 Solid Earth*, 84(B9), 4731–4735.
- 599 Jacobs, K., Savage, M., & Smith, E. (2016). Quantifying seismicity associated with
600 slow slip events in the Hikurangi margin, New Zealand. *New Zealand Journal
601 of Geology and Geophysics*, 59(1), 58–69.
- 602 King, P. R., & Thrasher, G. P. (1996). *Cretaceous-Cenozoic geology and petroleum
603 systems of the Taranaki Basin, New Zealand* (Vol. 2). Institute of Geological &
604 Nuclear Sciences.
- 605 Kodaira, S., Takahashi, N., Nakanishi, A., Miura, S., & Kaneda, Y. (2000). Sub-
606 ducted seamount imaged in the rupture zone of the 1946 Nankaido earthquake.
607 *Science*, 289(5476), 104–106.
- 608 Lewis, K., & Pettinga, J. (1993). The emerging, imbricate frontal wedge of the Hiku-
609 rangi margin. *Sedimentary Basins of the World*, 2, 225–250.
- 610 Lewis, K. B., Carter, L., & Davey, F. J. (1994). The opening of Cook Strait: inter-
611 glacial tidal scour and aligning basins at a subduction to transform plate edge.
612 *Marine Geology*, 116(3-4), 293–312.

- Lewis, K. B., Collot, J.-Y., & Lallem, S. E. (1998). The dammed Hikurangi Trough: a channel-fed trench blocked by subducting seamounts and their wake avalanches (New Zealand–France GeodyNZ Project). *Basin Research*, 10(4), 441–468.
- Litchfield, N., Ellis, S., Berryman, K., & Nicol, A. (2007). Insights into subduction-related uplift along the Hikurangi Margin, New Zealand, using numerical modeling. *Journal of Geophysical Research: Earth Surface*, 112(F2).
- Litchfield, N., Van Dissen, R., Sutherland, R., Barnes, P., Cox, S., Norris, R., ... others (2014). A model of active faulting in New Zealand. *New Zealand Journal of Geology and Geophysics*, 57(1), 32–56.
- Marcaillou, B., Collot, J.-Y., Ribodetti, A., d'Acremont, E., Mahamat, A.-A., & Alvarado, A. (2016). Seamount subduction at the North-Ecuadorian convergent margin: Effects on structures, inter-seismic coupling and seismogenesis. *Earth and Planetary Science Letters*, 433, 146–158.
- Mitchell, J. S., Mackay, K. A., Neil, H. L., Mackay, E. J., Pallentin, A., & Notman, P. (2012). *Undersea New Zealand, 1:5,000,000*. Retrieved from <https://niwa.co.nz/our-science/oceans/bathymetry/download-the-data>
- Modrak, R., & Tromp, J. (2016). Seismic waveform inversion best practices: regional, global and exploration test cases. *Geophysical Journal International*, 206(3), 1864–1889.
- Mortimer, N. (2004). New Zealand's geological foundations. *Gondwana research*, 7(1), 261–272.
- Nicol, A., Mazengarb, C., Chanier, F., Rait, G., Uruski, C., & Wallace, L. (2007). Tectonic evolution of the active Hikurangi subduction margin, New Zealand, since the Oligocene. *Tectonics*, 26(4).
- Pedley, K. L., Barnes, P. M., Pettinga, J. R., & Lewis, K. B. (2010). Seafloor structural geomorphic evolution of the accretionary frontal wedge in response to seamount subduction, Poverty Indentation, New Zealand. *Marine Geology*, 270(1-4), 119–138.
- Reyes, A., Christenson, B., & Faure, K. (2010). Sources of solutes and heat in low-enthalpy mineral waters and their relation to tectonic setting, New Zealand. *Journal of Volcanology and Geothermal Research*, 192(3-4), 117–141.
- Reyners, M., Eberhart-Phillips, D., & Bannister, S. (2017). Subducting an old subduction zone sideways provides insights into what controls plate coupling. *Earth and Planetary Science Letters*, 466, 53–61.
- Scholz, C. H., & Small, C. (1997). The effect of seamount subduction on seismic coupling. *Geology*, 25(6), 487–490.
- Singh, S. C., Hananto, N., Mukti, M., Robinson, D. P., Das, S., Chauhan, A., ... others (2011). Aseismic zone and earthquake segmentation associated with a deep subducted seamount in Sumatra. *Nature Geoscience*, 4(5), 308–311.
- Sun, T., Saffer, D., & Ellis, S. (2020). Mechanical and hydrological effects of seamount subduction on megathrust stress and slip. *Nature Geoscience*, 13(3), 249–255.
- Tao, K., Grand, S. P., & Niu, F. (2018). Seismic structure of the upper mantle beneath eastern Asia from full waveform seismic tomography. *Geochemistry, Geophysics, Geosystems*, 19(8), 2732–2763.
- Von Huene, R., & Scholl, D. W. (1991). Observations at convergent margins concerning sediment subduction, subduction erosion, and the growth of continental crust. *Reviews of Geophysics*, 29(3), 279–316.
- Wallace, L. (2020). Slow slip events in New Zealand. *Annual Review of Earth and Planetary Sciences*, 48, 175–203.
- Wallace, L., Barnes, P., Beavan, J., Van Dissen, R., Litchfield, N., Mountjoy, J., ... Pondard, N. (2012). The kinematics of a transition from subduction to strike-slip: An example from the central New Zealand plate boundary. *Journal of Geophysical Research: Solid Earth*, 117(B2).

- 668 Wallace, L., Beavan, J., Bannister, S., & Williams, C. (2012). Simultaneous long-
669 term and short-term slow slip events at the Hikurangi subduction margin,
670 New Zealand: Implications for processes that control slow slip event occur-
671 rence, duration, and migration. *Journal of Geophysical Research: Solid Earth*,
672 117(B11).
- 673 Wallace, L., Beavan, J., McCaffrey, R., & Darby, D. (2004). Subduction zone cou-
674 pling and tectonic block rotations in the North Island, New Zealand. *Journal*
675 *of Geophysical Research: Solid Earth*, 109(B12).
- 676 Wallace, L., Reyners, M., Cochran, U., Bannister, S., Barnes, P., Berryman, K.,
677 ... Power, W. (2009). Characterizing the seismogenic zone of a major plate
678 boundary subduction thrust: Hikurangi Margin, New Zealand. *Geochemistry,*
679 *Geophysics, Geosystems*, 10(10). doi: 10.1029/2009GC002610
- 680 Wang, K., & Bilek, S. L. (2011). Do subducting seamounts generate or stop large
681 earthquakes? *Geology*, 39(9), 819–822.
- 682 Warren-Smith, E., Fry, B., Wallace, L., Chon, E., Henrys, S., Sheehan, A., ... Lebe-
683 dev, S. (2019). Episodic stress and fluid pressure cycling in subducting oceanic
684 crust during slow slip. *Nature Geoscience*, 12(6), 475–481.
- 685 Williams, C., Eberhart-Phillips, D., Bannister, S., Barker, D., Henrys, S., Reyners,
686 M., & Sutherland, R. (2013). Revised interface geometry for the Hikurangi
687 subduction zone, New Zealand. *Seismological Research Letters*, 84(6), 1066–
688 1073.
- 689 Wilson, C., Gravley, D., Leonard, G., & Rowland, J. (2009). Volcanism in the cen-
690 tral Taupo Volcanic Zone, New Zealand: tempo, styles and controls. *Studies in*
691 *Volcanology: the Legacy of George Walker. Special Publications of IAVCEI*, 2,
692 225–247.
- 693 Wilson, C., Houghton, B., McWilliams, M., Lanphere, M., Weaver, S., & Briggs,
694 R. (1995). Volcanic and structural evolution of Taupo Volcanic Zone, New
695 Zealand: a review. *Journal of Volcanology and Geothermal Research*, 68(1-3),
696 1–28.
- 697 Yang, H., Liu, Y., & Lin, J. (2013). Geometrical effects of a subducted seamount
698 on stopping megathrust ruptures. *Geophysical Research Letters*, 40(10), 2011–
699 2016.
- 700 Zhu, H., Bozdağ, E., & Tromp, J. (2015). Seismic structure of the European up-
701 per mantle based on adjoint tomography. *Geophysical Journal International*,
702 201(1), 18–52.